

Faraday Rotation Spectroscopy of Quantum-Dot Quantum Wells

Florian Meier and David D. Awschalom
Center for Spintronics and Quantum Computation,

University of California, Santa Barbara, California 93106, USA

(Dated: September 21, 2018)

Time-resolved Faraday rotation studies of CdS/CdSe/CdS quantum-dot quantum wells have recently shown that the Faraday rotation angle exhibits several well-defined resonances as a function of probe energy close to the absorption edge. Here, we calculate the Faraday rotation angle from the eigenstates of the quantum-dot quantum well obtained with $\mathbf{k} \cdot \mathbf{p}$ theory. We show that the large number of narrow resonances with comparable spectral weight observed in experiment is not reproduced by the level scheme of a quantum-dot quantum well with perfect spherical symmetry. A simple model for broken spherical symmetry yields results in better qualitative agreement with experiment.

PACS numbers: 78.67.Hc, 73.22.-f, 78.20.Ls

I. INTRODUCTION

Semiconductor heterostructures with a size of several nanometers, such as core-shell quantum dots, have been widely studied in the past years. The combination of several semiconducting materials in a single nanocrystal provides additional degrees of freedom which allow one to tailor the properties of nanocrystals to a certain extent.^{1,2} Capping layers of a high-bandgap material on a low-bandgap quantum dot (QD) passivate the surface and increase the optical gain.^{3,4} Quantum-dot quantum wells (QDQWs), with several layers of a low-bandgap material sandwiched between a high-bandgap core and cap are not only of interest from a fundamental point of view,^{5,6,7,8,9,10} but could also be scaled up to functional heterostructures in a single nanometer-size object.

Although QDQWs have been studied for several years, a detailed investigation of the quantum size spectrum using photoluminescence (PL) or absorption spectroscopy is challenging because of inhomogeneous broadening. PL typically shows a single broad peak, while the absorption spectrum exhibits a staircase-like spectrum without distinct resonances. Individual exciton transitions have been observed using techniques such as hole burning where a homogeneous subset of QDQWs is probed selectively.⁷ Time-resolved Faraday rotation (TRFR), a well-established technique to investigate the spin dynamics in nanocrystals,^{11,12} has recently been used to characterize colloidal CdS/CdSe/CdS QDQWs with hexagonal wurtzite crystal structure.¹³ The TRFR signal amplitude was found to depend sensitively on probe energy and to exhibit three resonances with linewidths as small as 10 – 20 meV within an energy window of 0.2 eV around the absorption edge. Hence, TRFR does not only provide information on the spin dynamics, but also is a sensitive spectroscopic technique which allows one to identify individual exciton transitions in QDQWs.

Here, we develop a microscopic theory for the TRFR signal amplitude as a function of probe energy for QDQWs. From the eigenstates calculated using a two- and four-band $\mathbf{k} \cdot \mathbf{p}$ description for the conduction and va-

lence band states, respectively, we determine the dynamic dielectric response functions for σ^\pm circularly polarized light and the amplitude of the TRFR signal, $\theta_F(E)$. While several narrow resonances in $\theta_F(E)$ are predicted and the resonance energies are well reproduced by $\mathbf{k} \cdot \mathbf{p}$ theory, our calculations show that the spectral weight of the resonances detected experimentally¹³ is not reproduced by the level scheme of a spherical QDQW (Sec. II). We discuss a simple model in which deformation of the QDQW leads to mixing of valence band multiplets, such that spectral weight is re-distributed between the different dipole-allowed exciton transitions. Our calculations show that this model yields better qualitative agreement with experimental data and may provide a possible explanation for the well-defined resonances in the TRFR signal and the featureless increase in the absorption signal (Sec. III). In Sec. IV, we summarize our results.

II. SPHERICAL QDQWS

A. Energy level scheme

We first consider CdS/CdSe/CdS QDQWs with perfect spherical symmetry as shown in Figs. 1(a), (b). The CdS/CdSe/CdS QDQWs have hexagonal wurtzite crystal structure. For the QDQWs in Ref. 13, the radius of the CdS core and the width of the CdS cap are $r_1 \simeq 1.7$ nm and $r_3 - r_2 \simeq 1.6$ nm, respectively. The width of the CdSe quantum well (QW), $r_2 - r_1 = n_{\text{CdSe}} a_{\text{CdSe}}$, is estimated from the number of CdSe monolayers, n_{CdSe} , and the monolayer thickness in bulk CdSe, $a_{\text{CdSe}} \simeq 0.43$ nm.¹⁴ Because the focus of this paper is the TRFR signal amplitude as a function of probe energy, we restrict ourselves to the simplest realistic description of the QDQW. The energy levels are calculated from $\mathbf{k} \cdot \mathbf{p}$ theory,^{15,16} with a two-band Hamiltonian for the conduction band states and a four-band Luttinger Hamiltonian for the heavy and light hole valence band states.

In the two-band approximation, the conduction band

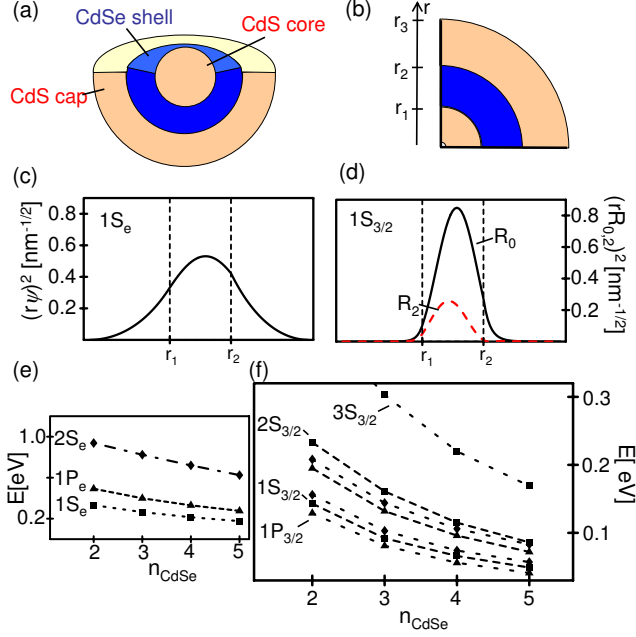


FIG. 1: (color online). (a) Schematic representation of the CdS/CdSe/CdS QDQW of Ref. 13. (b) The radius of the central CdS core is denoted by r_1 , the width of the CdSe QW by $r_2 - r_1$, and the width of the CdS cap by $r_3 - r_2$. Numerical values are given in the text. (c) Radial probability distribution of the conduction band ground state $1S_e$. Because of the small conduction band mass, the state is not well localized in the QW (indicated by dashed vertical lines). (d) Radial probability distribution of the $1S_{3/2}$ valence band state. The two components of the wave function, R_0 and R_2 , are shown in solid and dashed lines, respectively. Because the valence band mass is large compared to the conduction band mass, the valence band states are more strongly localized in the QW. (e) Energies of the $1S_e$, $2S_e$, and $1P_e$ conduction band levels as a function of QW width. (f) Energies of the lowest three valence band levels with $S_{3/2}$ -symmetry (squares) as a function of QW width. The energies of the states $1P_{3/2}$, $1D_{5/2}$, $1P_{5/2}$, and $1D_{7/2}$ are also shown (from bottom). Labels for $1D_{5/2}$, $1P_{5/2}$, and $1D_{7/2}$ are omitted for clarity.

states are determined by

$$\hat{H}_{cb} = \hat{\mathbf{k}} \frac{1}{2m(r)} \hat{\mathbf{k}} + V_c(r), \quad (1)$$

where the band mass is given by the value of bulk CdSe and CdS, respectively,¹⁷

$$m(r) = \begin{cases} m_{\text{CdSe}} = 0.11 m_0, & r_1 < r < r_2, \\ m_{\text{CdS}} = 0.15 m_0, & r < r_1 \text{ or } r > r_2. \end{cases} \quad (2)$$

m_0 denotes the free electron mass and $\hat{\mathbf{k}}$ the momentum operator for the envelope wave function. The potential $V_c(r)$ in \hat{H}_{cb} represents the offset of the CdS conduction band relative to CdSe, 0.32 eV.¹⁸ Vanishing boundary conditions are imposed at r_3 . In Fig. 1(e), the $1S_e$, $2S_e$,

and $1P_e$ energy levels are displayed as a function of QW width. Figure 1(c) shows the radial probability distribution for the conduction band ground state, $1S_e$, for $n_{\text{CdSe}} = 3$. Because of the small conduction band mass, the state is not well localized in the QW. The lattice mismatch at the CdS/CdSe interface (4%) is expected to also modify the electronic band structure,¹⁹ an effect that is neglected in our calculations. While the detailed band structure close to the interface is not fully understood, a likely scenario is that the lattice constant varies gradually, giving rise to band realignment and a gradual change in the radial potential $V_c(r)$ rather than the step-like behavior considered here.

In the spherical approximation, heavy and light hole valence band states are determined by the Luttinger Hamiltonian

$$\hat{H}_{vb} = [\gamma_1(r) + \frac{5}{2}\gamma(r)] \frac{\hat{\mathbf{k}}^2}{2m_0} - \frac{\gamma(r)}{m_0} (\hat{\mathbf{k}} \cdot \hat{\mathbf{J}})^2 + V_v(r) \quad (3)$$

for $r \neq r_{1,2}$. $\hat{\mathbf{J}}$ denotes the spin operator of the $J = 3/2$ valence band multiplet. States of the $J = 1/2$ split-off band are offset in energy by 0.4 eV and are neglected in the following. $\gamma_1(r)$ and $\gamma(r)$ are the Luttinger parameters of CdSe (CdS) for r inside (outside) the QW,^{17,20,21}

$$\gamma_1(r) = \begin{cases} \gamma_{1,\text{CdSe}} = 1.67, & r_1 < r < r_2; \\ \gamma_{1,\text{CdS}} = 1.09, & r < r_1 \text{ or } r > r_2, \end{cases} \quad (4)$$

and

$$\gamma(r) = \begin{cases} \gamma_{\text{CdSe}} = 0.56, & r_1 < r < r_2; \\ \gamma_{\text{CdS}} = 0.34, & r < r_1 \text{ or } r > r_2. \end{cases} \quad (5)$$

Because $\hat{\mathbf{k}}$ does not commute with $\gamma_1(r)$ and $\gamma(r)$, operator ordering in Eq. (3) is important for $r = r_{1,2}$ (see Ref. 16 and references therein) and will be specified by the boundary conditions at the interfaces in Eq. (8) below. $V_v(r)$ represents the offset of 0.42 eV of the CdS valence band edge relative to CdSe.¹⁸

The eigenstates of \hat{H}_{vb} have been explicitly calculated for both QDs^{22,23} and QDQWs.^{15,16} While the orbital angular momentum $\hat{\mathbf{L}}$ of the envelope wave function is no longer a good quantum number, the sum of orbital and spin angular momentum, $\hat{\mathbf{F}} = \hat{\mathbf{L}} + \hat{\mathbf{J}}$, commutes with the Hamiltonian, $[\hat{H}_{vb}, \hat{\mathbf{F}}] = 0$. Eigenstates of \hat{H}_{vb} are labelled according to the quantum numbers F , F_z , and the smallest angular momentum component L of the envelope wave function. The eigenstates^{22,23}

$$|nL_F; F_z\rangle = R_L(r) |L, \frac{3}{2}, F, F_z\rangle + R_{L+2}(r) |L+2, \frac{3}{2}, F, F_z\rangle \quad (6)$$

are superpositions of envelope functions with angular momentum L and $L+2$. For $r < r_1$, $r_1 < r < r_2$, and $r_2 < r$, the radial wave functions $R_L(r)$ and $R_{L+2}(r)$ are solutions of the differential equations²²

$$\begin{pmatrix} -\frac{\hbar^2}{2m_0}(\gamma_1 + c_1\gamma) \left(\partial_r^2 + \frac{2}{r}\partial_r - \frac{L(L+1)}{r^2} \right) + V_v(r) & c_2\gamma \frac{\hbar^2}{2m_0} \left(\partial_r^2 + \frac{2L+5}{r}\partial_r + \frac{(L+1)(L+3)}{r^2} \right) \\ c_2\gamma \frac{\hbar^2}{2m_0} \left(\partial_r^2 - \frac{2L+1}{r}\partial_r + \frac{L(L+2)}{r^2} \right) & -\frac{\hbar^2}{2m_0}(\gamma_1 - c_1\gamma) \left(\partial_r^2 + \frac{2}{r}\partial_r - \frac{(L+2)(L+3)}{r^2} \right) + V_v(r) \end{pmatrix} \begin{pmatrix} R_L \\ R_{L+2} \end{pmatrix} = E \begin{pmatrix} R_L \\ R_{L+2} \end{pmatrix}. \quad (7)$$

The full Hamiltonian with the correct operator ordering at $r = r_{1,2}$ is given, e.g., in Ref. 16 and is omitted here for brevity. The dimensionless constants $c_{1,2}$ depend on F and L and can be read off from the values $C_{1,2}$ in Table I of Ref. 22 with the correspondence $c_{1,2} = 2C_{1,2}/\mu$. Equation (7) is solved with a piecewise ansatz in the spherical Bessel functions j_L and n_L . The boundary conditions for the derivatives require that

$$\begin{pmatrix} \gamma_1\partial_r + c_1\gamma \left(\partial_r + \frac{3}{2r} \right) & -c_2\gamma \left(\partial_r + \frac{L+3}{r} \right) \\ -c_2\gamma \left(\partial_r - \frac{L}{r} \right) & \gamma_1\partial_r - c_1\gamma \left(\partial_r + \frac{3}{2r} \right) \end{pmatrix} \times \begin{pmatrix} R_L \\ R_{L+2} \end{pmatrix} \quad (8)$$

is continuous at $r_{1,2}$.¹⁶

We have calculated the lowest conduction and valence band energy levels for the QDQWs of Ref. 13. The wave functions of the conduction band ground state, $1S_e$, and the components $R_{0,2}$ of $1S_{3/2}$ are shown in Figs. 1(c) and (d), respectively. The lowest valence band states are (in order of increasing energy) $1P_{3/2}$, $1S_{3/2}$, $1D_{5/2}$, and $1P_{5/2}$ [Fig. 1(f)]. Similarly to CdS/HgS/CdS QDQWs,^{15,16,24,25} the envelope function of the valence band ground state is p -type, implying a dark exciton ground state. While the conduction band states are strongly delocalized over core, QW, and cap, the valence band states are much better localized in the QW because of the larger valence band mass.

The electron-hole Coulomb attraction is calculated in first order perturbation theory because the QDQWs are in the strong-confinement regime. We neglect the small difference in dielectric constants for CdS and CdSe and set $\epsilon = \epsilon_{\text{CdSe}} = \epsilon_{\text{CdS}} = 9$. For an electron in the conduction band ground state, $1S_e$, the exciton binding energy U is

$$U = -\frac{e^2}{4\pi\epsilon\epsilon_0} \int_0^{r_3} dr_e dr_h \frac{r_e^2 r_h^2}{\max(r_e, r_h)} \psi_{1S_e}(r_e)^2 \times [R_L(r_h)^2 + R_{L+2}(r_h)^2], \quad (9)$$

with $\psi_{1S_e}(r_e)$ the radial wave function of $1S_e$ and $R_{L,L+2}$ the radial components of the hole state. For both the $1P_{3/2}$ and the $1S_{3/2}$ multiplet, the Coulomb integral is well approximated by $U = -e^2/4\pi\epsilon\epsilon_0[(r_1 + r_2)/2]$. The calculation of the dynamic dielectric response functions in Sec. II B involves virtual transitions from one-exciton to bi-exciton states, such that the bi-exciton shift must be evaluated. For a bi-exciton with two electrons in $1S_e$

and two holes in $1S_{3/2}$, the bi-exciton shift is of order 5 meV, sufficiently small that it can be neglected in the following. Similarly, the electron-hole exchange interaction is neglected because its characteristic energy scale is of order 1 meV.²⁶

The lattice anisotropy of the wurtzite crystal structure is taken into account by the anisotropy Hamiltonian²³

$$\hat{H}_{\text{an}} = \Delta \left[(3/2)^2 - \hat{J}_z^2 \right]. \quad (10)$$

Because the hole wave functions are localized predominantly in the CdSe QW, we approximate $\Delta = 25$ meV by the CdSe bulk value.^{23,27} \hat{H}_{an} lifts the degeneracy of an L_F -multiplet and splits it into $(2F+1)/2$ energy doublets. In particular, for $S_{3/2}$ multiplets, the energy shifts induced by \hat{H}_{an} are²⁷

$$\begin{aligned} \Delta_{n,3/2} &= \langle nS_{3/2}; 3/2 | \hat{H}_{\text{an}} | nS_{3/2}; 3/2 \rangle \quad (11a) \\ &= \Delta \frac{4}{5} \int dr r^2 R_2^2, \end{aligned}$$

$$\begin{aligned} \Delta_{n,1/2} &= \langle nS_{3/2}; 1/2 | \hat{H}_{\text{an}} | nS_{3/2}; 1/2 \rangle \quad (11b) \\ &= \Delta \left[\int dr r^2 R_0^2 + \frac{1}{5} \int dr r^2 R_2^2 \right] \end{aligned}$$

for $|F_z| = 3/2$ and $|F_z| = 1/2$, respectively.

B. Faraday rotation angle

We next calculate the amplitude of the Faraday rotation (FR) angle as a function of probe energy, $\theta_F(E)$, taking into account the single-particle levels, Coulomb interaction, and crystal anisotropy as described in Sec. II A. In the pump-probe scheme of Ref. 13, a σ^- circularly polarized pump pulse with energy large compared to the absorption edge excites spin-polarized excitons. While the conduction band electron typically retains its spin polarization on relaxation to the conduction band ground state, $1S_e$, the hole spin is believed to randomize quickly during relaxation to $1P_{3/2}$. The net spin polarization along the pump direction, which results from conduction band electrons in the spin state $|s_z = \uparrow\rangle$, is experimentally detected with TRFR. For probe energy E , $\theta_F(E)$ is proportional to the difference of the dynamic dielectric response functions for σ^\pm circularly polarized light, $\epsilon_+(E/\hbar) - \epsilon_-(E/\hbar)$, which are determined by the optical

dipole transition matrix elements,^{28,29,30,31}

$$\theta_F(E) = CE \sum_{\sigma=\pm 1; |XX\rangle} \sigma |\langle XX | \hat{p}_x + \sigma i \hat{p}_y | X_{\text{in}} \rangle|^2 \times \frac{E - (E_{XX} - E_{X_{\text{in}}})}{(E_{XX} - E_{X_{\text{in}}})^2 + \gamma_{XX}^2}. \quad (12)$$

$|X_{\text{in}}\rangle$ denotes the initial $1S_e - 1P_{3/2}$ exciton prepared by the pump pulse with an $|s_z = \uparrow\rangle$ -electron in $1S_e$. The sum extends over all bi-exciton states $|XX\rangle$ with energy E_{XX} , and γ_{XX} denotes the linewidth of the corresponding bi-exciton transition. For simplicity, we assume that the linewidth of all transitions is equal, $\gamma_{XX} = \Gamma$. The constant C depends on the sample size and refractive index. $\theta_F(E)$ is finite because transitions to bi-exciton states with both conduction band electrons in $1S_e$ are allowed only if the electrons form a singlet state. Hence, the matrix elements in Eq. (12) can be expressed in terms of the transitions from an arbitrary valence band state $|\Phi_v\rangle$ to the unoccupied conduction band state $|1S_e; \downarrow\rangle$,

$$\theta_F(E) = CE \sum_{\sigma=\pm 1; |\Phi_v\rangle} \sigma |\langle 1S_e; \downarrow | \hat{p}_x + \sigma i \hat{p}_y | \Phi_v \rangle|^2 \times \frac{E - E_{X,v}}{(E - E_{X,v})^2 + \Gamma^2}, \quad (13)$$

with $E_{X,v}$ the energy of the $1S_e - \Phi_v$ exciton. As mentioned in Sec. II A, the bi-exciton shift is negligible. This expression depends only on the single-particle levels in the conduction and valence band and can be evaluated from the wave functions calculated above.

The dipole transition matrix elements are evaluated following Ref. 23. The overlap integral of the envelope wave functions is finite only for s -type valence band states, $|\Phi_v\rangle = |nS_{3/2}; F_z\rangle$. We first consider a QDQW with crystal symmetry axis aligned along the laser direction. Then,

$$|\langle 1S_e; \downarrow | \hat{p}_x - i \hat{p}_y | nS_{3/2}; F_z \rangle|^2 \quad (14a)$$

$$= \frac{2}{3} \left| \int dr r^2 \psi_{1S_e} R_0 \langle S | \hat{p}_z | Z \rangle \right|^2 \delta_{F_z, 1/2} \\ \simeq \frac{2}{3} (m_0 V)^2 \left| \int dr r^2 \psi_{1S_e} R_0 \right|^2 \delta_{F_z, 1/2},$$

$$|\langle 1S_e; \downarrow | \hat{p}_x + i \hat{p}_y | nS_{3/2}; F_z \rangle|^2 \quad (14b)$$

$$= 2 \left| \int dr r^2 \psi_{1S_e} R_0 \langle S | \hat{p}_z | Z \rangle \right|^2 \delta_{F_z, -3/2} \\ \simeq 2 (m_0 V)^2 \left| \int dr r^2 \psi_{1S_e} R_0 \right|^2 \delta_{F_z, -3/2},$$

while the matrix elements vanish for $F_z = 3/2, -1/2$. The Kane interband matrix element $\langle S | \hat{p}_z | Z \rangle$ varies spatially for the QDQW, but because the valence band states are well localized in the CdSe QW, we approximate $|\langle S | \hat{p}_z | Z \rangle| \simeq m_0 V$ by the CdSe interband matrix

n_{CdSe}	3	4	5
I_1	0.60	0.67	0.72
I_2	0.16	0.11	0.08
I_3	0.09	0.09	0.10

TABLE I: Radial overlap integrals, Eq. (15), for $1S_{3/2}$, $2S_{3/2}$, and $3S_{3/2}$ valence band states as a function of the QW width, n_{CdSe} .

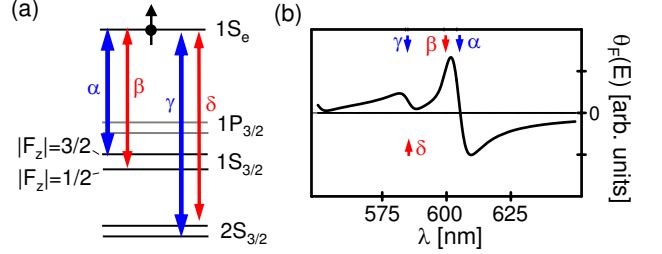


FIG. 2: (color online). (a) Schematic representation of the transitions which contribute to the FR angle, $\theta_F(E)$, in the spectral representation Eq. (13). The dipole transition matrix elements with $1S_e$ are finite only for $S_{3/2}$ -multiplets. (b) $\theta_F(E)$ calculated from Eq. (16) for $n_{\text{CdSe}} = 3$ and $\Gamma = 15$ meV. $nS_{3/2}$ multiplets with $n \geq 4$ have been neglected. The transitions from (a) are indicated by arrows.

element. The overlap integral in Eq. (14), in the following denoted by

$$I_n = \left| \int dr r^2 \psi_{1S_e} R_0 \right|^2, \quad (15)$$

depends on the quantum number n via R_0 . For $1S_{3/2}$, $2S_{3/2}$, and $3S_{3/2}$, the numerical values are given in Table I for different QW widths.

With the transition matrix elements, $\theta_F(E)$ is readily evaluated for E close to the absorption edge. We define the energy $E_{X,n} = E_{1S_e} + E_{nS_{3/2}} + E_g + U$ of the $1S_e - nS_{3/2}$ exciton, where $E_g \simeq 1.75$ eV is the bandgap of bulk CdSe at room temperature and U the Coulomb integral [Eq. (9)]. Combining Eqs. (13) and (14),

$$\theta_F(E) \simeq C' E \sum_n I_n \left[\frac{E - (E_{X,n} + \Delta_{n,3/2})}{[E - (E_{X,n} + \Delta_{n,3/2})]^2 + \Gamma^2} - \frac{1}{3} \frac{E - (E_{X,n} + \Delta_{n,1/2})}{[E - (E_{X,n} + \Delta_{n,1/2})]^2 + \Gamma^2} \right], \quad (16)$$

where $C' = 2C(m_0 V)^2$ and E was assumed to be sufficiently close to the absorption edge that transitions from the split-off band can be neglected. The energy shifts $\Delta_{n,3/2}$ and $\Delta_{n,1/2}$ are induced by the structural anisotropy [Eq. (11)].

For every valence band multiplet $nS_{3/2}$, $\theta_F(E)$ shows a double-resonance structure, with a main resonance corresponding to transitions from $|F_z| = 3/2$ [first term in the square bracket in Eq. (16)] and a second resonance with $1/3$ smaller spectral weight that corresponds

to transitions from $|F_z| = 1/2$ states and is shifted by $\Delta_{n,1/2} - \Delta_{n,3/2}$. The second resonance can only be resolved if $\Gamma < \Delta$. For the colloidal QDQWs in Ref. 13, the inhomogeneous line broadening is substantial, $\Gamma \gtrsim 15$ meV, and the splitting of resonances caused by crystal anisotropy cannot be resolved. The lowest transitions with finite matrix elements in the spectral representation in Eq. (13) are shown schematically in Fig. 2(a). Figure 2(b) shows $\theta_F(E)$ close to the absorption edge for $n_{\text{CdSe}} = 3$. While resonances corresponding to $1S_{3/2}$, $2S_{3/2}$, and $3S_{3/2}$ can be resolved, the spectral weight for $1S_{3/2}$ is significantly larger than that for $2S_{3/2}$ and $3S_{3/2}$. The behavior in Fig. 2(b) is clearly distinct from experimental data¹³ which exhibit three resonances with comparable spectral weight within 0.2 eV of the absorption edge.

We next calculate $\theta_F(E)$ for the case that the QDQW symmetry axis is not aligned with the laser. By averaging over different relative orientations, we also determine $\theta_F(E)$ for an ensemble of randomly oriented QDQWs. If the QDQW crystal symmetry axis is tilted by ψ relative to the laser propagation direction, the electric field components of the pump and probe laser pulses, given in the laboratory coordinate system (indicated with a superscript L in the following), are rotated relative to the spin quantization axis of the QDQW. The spectral representation for $\theta_F(E)$ is still given by Eq. (13), but the matrix elements must be modified to $\langle 1S_e; \downarrow^L | \hat{p}_x^L + \sigma i \hat{p}_y^L | \Phi_v \rangle$ to account for the fact that the pump and probe pulses are defined in the laboratory coordinate system L . To evaluate the matrix elements, operators in the L -frame are expressed in terms of the QDQW coordinate system, $|\downarrow^L\rangle = i \sin(\psi/2) |\uparrow\rangle + \cos(\psi/2) |\downarrow\rangle$, $\hat{p}_x^L = \cos(\psi) \hat{p}_x + \sin(\psi) \hat{p}_z$, and $\hat{p}_y^L = \hat{p}_y$. With the convention for the valence band basis functions in Refs. 27,32,

$$\langle 1S_e; \downarrow^L | \hat{p}_x^L \pm i \hat{p}_y^L | nS_{3/2}; F_z \rangle = \sqrt{I_n/2} m_0 V \quad (17)$$

$$\times \begin{cases} -i \sin(\psi/2) [\cos(\psi) \mp 1], & F_z = 3/2; \\ -(2/\sqrt{3}) \sin(\psi/2) \sin(\psi) & F_z = 1/2; \\ + (i/\sqrt{3}) \cos(\psi/2) [\cos(\psi) \mp 1], \\ (2/\sqrt{3}) \cos(\psi/2) \sin(\psi) & F_z = -1/2; \\ - (i/\sqrt{3}) \sin(\psi/2) [\cos(\psi) \pm 1], \\ i \cos(\psi/2) [\cos(\psi) \pm 1], & F_z = -3/2. \end{cases}$$

Inserting these transition matrix elements into the spectral representation in Eq. (13), we find that the expression for $\theta_F(E)$ only acquires a pre-factor $\cos^2(\psi/2) \cos(\psi)$,

$$\theta_F(E) \simeq C' E \cos^2(\psi/2) \cos(\psi) \quad (18)$$

$$\times \sum_n I_n \left[\frac{E - (E_{X,n} + \Delta_{n,3/2})}{[E - (E_{X,n} + \Delta_{n,3/2})]^2 + \Gamma^2} - \frac{1}{3} \frac{E - (E_{X,n} + \Delta_{n,1/2})}{[E - (E_{X,n} + \Delta_{n,1/2})]^2 + \Gamma^2} \right],$$

but the relative weight of the individual terms is not altered. In particular, Eq. (18) implies $\theta_F = 0$ for $\psi = \pi/2$. This can be understood in physical terms because TRFR probes the spin polarization along the QDQW anisotropy axis, while, for $\psi = \pi/2$, the pump pulse only generates spin polarization perpendicular to the anisotropy axis.

Averaging Eq. (18) over an ensemble of randomly oriented QDQWs is performed by integration over ψ . For random QDQW orientation, Eq. (16) remains valid with the substitution $C' \rightarrow 5C'/12$. While random QDQW orientation reduces the total amplitude of $\theta_F(E)$, the relative spectral weight of the individual contributions is not altered and $\theta_F(E)$ is still as shown in Fig. 2(b).

III. BROKEN SPHERICAL SYMMETRY

The calculations in Sec. II above show that, for a spherical QDQW, $\theta_F(E)$ exhibits a pair of resonances for every $nS_{3/2} - 1S_e$ exciton transition. However, the spectral weight of the resonances decreases rapidly with increasing n (Table I), such that the large number of resonances with comparable spectral weight observed experimentally¹³ is not correctly reproduced by Eq. (16). The experimental data imply that spectral weight is redistributed from the $1S_{3/2} - 1S_e$ exciton line to other transitions.

We show next that broken spherical symmetry is a possible mechanism which accounts for the experimental FR data by mixing of the $1S_{3/2}$ and $1P_{3/2}$ valence band multiplets. The admixture of s -type to p -type multiplets redistributes the spectral weight and increases the number of resonances with comparable amplitude in $\theta_F(E)$. As will be shown below, the redistribution of spectral weight also explains the absence of pronounced resonances in the absorption signal. Compared to spherical QDQWs, broken symmetry gives rise to a larger energy splitting between the lowest valence band states with dominant p -type and s -type envelope wave functions, consistent with the large Stokes shift between the PL peak and the absorption edge observed for CdS/CdSe/CdS QDQWs.^{10,13}

On a microscopic level, broken spherical symmetry would most probably result from a spatial variation of the QW width [shown schematically in Fig. 3(a)]. For QWs with $n_{\text{CdSe}} = 2, 3, 4, 5$, a monolayer variation in QW width translates into a perturbation with a typical energy scale of order 0.1 eV for the hole states. Conduction band states are less strongly affected because they are not localized in the QW and the energy level spacing is much larger. We do not attempt to describe breaking of the spherical symmetry microscopically, but restrict our discussion to a simple model in which the valence band Hamiltonian includes a potential

$$\delta V(\mathbf{r}) = v_0 \sin \theta (1 + \cos \phi) \quad (19)$$

which mixes $1S_{3/2}$ and $1P_{3/2}$. θ and ϕ denote the azimuthal and polar angle of \mathbf{r} relative to the lattice symmetry axis, respectively. v_0 is a fit parameter.

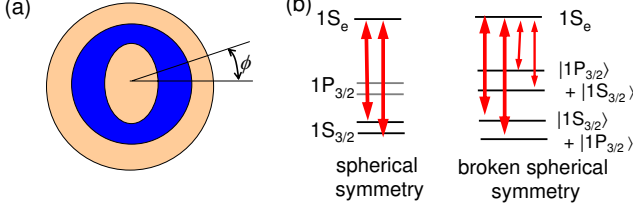


FIG. 3: (color online). (a) Cross section of a QDQW with broken spherical symmetry. A deformation of the central CdS QD implies a spatial variation of the QW width, which is modelled by Eq. (19). (b) Schematic representation of the level scheme for a spherical QDQW and a QDQW with broken spherical symmetry. Broken spherical symmetry mixes the $1S_{3/2}$ and $1P_{3/2}$ multiplets and renders transitions to $1S_e$ bright for all eight states of the multiplet.

The exact hole states with the perturbation Eq. (19) can, at least in principle, be obtained by diagonalization of $\delta V(\mathbf{r})$ in the basis $|nL_F; F_z\rangle$ of the spherical system. The only finite matrix elements are $\langle n'L'_F; F'_z | \delta V(\mathbf{r}) | nL_F; F_z \rangle \propto \delta_{F_z, F'_z}$ for $|L-L'|$ an integer multiple of 2 and $\langle n'L'_F; F'_z | \delta V(\mathbf{r}) | nL_F; F_z \rangle \propto \delta_{F_z, F'_z \pm 1}$ for $|L-L'| = 1$ or $|L-L'| = 3$. In order to keep the subsequent discussion transparent, we restrict the diagonalization of $\delta V(\mathbf{r})$ to the subspace spanned by the valence band multiplets $1S_{3/2}$, $2S_{3/2}$, $3S_{3/2}$, and $1P_{3/2}$. These states are dominant for the optical response close to the absorption edge and we expect this procedure to qualitatively capture the essential features of broken spherical symmetry.³³

The off-diagonal matrix elements of $\delta V(\mathbf{r})$ between the $1S_{3/2}$ and $1P_{3/2}$ multiplet are calculated by expansion of the envelope wave functions in spherical harmonics. We find

$$\langle 1S_{3/2}; F'_z | \delta V(\mathbf{r}) | 1P_{3/2}; F_z \rangle = \frac{v_0}{\sqrt{15}} \times \int dr r^2 \left[R_0 R_1 + \frac{4}{5} R_2 R_1 + \frac{3}{5} R_2 R_3 \right] \quad (20)$$

for $(F'_z, F_z) = \pm(3/2, 1/2)$ or $\pm(1/2, 3/2)$, and

$$\langle 1S_{3/2}; F'_z | \delta V(\mathbf{r}) | 1P_{3/2}; F_z \rangle = \frac{v_0}{\sqrt{5}} \times \int dr r^2 \left[\frac{2}{3} R_0 R_1 + \frac{8}{15} R_2 R_1 + \frac{2}{5} R_2 R_3 \right] \quad (21)$$

for $(F'_z, F_z) = \pm(1/2, -1/2)$. The diagonal matrix elements $\langle 1S_{3/2}; F_z | \delta V(\mathbf{r}) | 1S_{3/2}; F_z \rangle = \pi v_0 / 4$ and $\langle 1P_{3/2}; F_z | \delta V(\mathbf{r}) | 1P_{3/2}; F_z \rangle \simeq \pi v_0 (9 + 2\delta_{|F_z|, 1/2}) / 40$ are evaluated analogously.

The energy eigenstates are calculated by diagonalization $\hat{H}_{vb} + \hat{H}_{an} + \delta V(\mathbf{r})$ in the eight-dimensional space spanned by the $1S_{3/2}$ and $1P_{3/2}$ multiplets. Mixing of $2S_{3/2}$ and $3S_{3/2}$ with $1P_{3/2}$ is neglected because of the large energy difference [Fig. 1(f)]. Because \hat{H}_{vb} , \hat{H}_{an} ,

and $\delta V(\mathbf{r})$ are even under reflection at the x - y -plane, the eigensystem consists of four doublets. The eigenstates

$$|\Psi_{v,i}^{(SP)}\rangle = \sum_{F_z=-3/2}^{3/2} (\alpha_{i,F_z} |1S_{3/2}; F_z\rangle + \beta_{i,F_z} |1P_{3/2}; F_z\rangle) \quad (22)$$

have components with s - and p -type envelope functions with expansion coefficients α_{i,F_z} and β_{i,F_z} , respectively. The corresponding energy eigenvalue is denoted by $E_{v,i}$.

The mixing of $1S_{3/2}$ and $1P_{3/2}$ multiplets renders transitions from all eight states $|\Psi_{v,i}^{(SP)}\rangle$ to $1S_e$ dipole-allowed [shown schematically in Fig. 3(b)]. Defining the energy of the $1S_e$ - $\Psi_{v,i}^{(SP)}$ exciton by E_{X_i} , for QDQWs with symmetry axes oriented along the laser beam, the spectral representation for $\theta_F(E)$ reads

$$\theta_F(E) \simeq C' E I_1 \sum_i \left(|\alpha_{i,-3/2}|^2 - \frac{|\alpha_{i,1/2}|^2}{3} \right) \times \frac{E - E_{X_i}}{(E - E_{X_i})^2 + \Gamma^2}, \quad (23)$$

$$+ C' E \sum_{n=2,3} I_n \left[\frac{E - (E_{X,n} + \tilde{\Delta}_{n,3/2})}{[E - (E_{X,n} + \tilde{\Delta}_{n,3/2})]^2 + \Gamma^2} - \frac{1}{3} \frac{E - (E_{X,n} + \tilde{\Delta}_{n,1/2})}{[E - (E_{X,n} + \tilde{\Delta}_{n,1/2})]^2 + \Gamma^2} \right],$$

where the sum i extends over the states $|\Psi_{v,i}^{(SP)}\rangle$. For the $2S_{3/2}$ and $3S_{3/2}$ valence band multiplets [third and fourth line of Eq. (23)], $\tilde{\Delta}_{n,F_z} = \Delta_{n,F_z} + \langle nS_{3/2}; F_z | \delta V(\mathbf{r}) | nS_{3/2}; F_z \rangle$ takes into account the energy shifts effected by the lattice anisotropy \hat{H}_{an} and the shape anisotropy $\delta V(\mathbf{r})$ to first order. For $v_0 = 0$, this expression correctly simplifies to the one obtained for the spherical system.

In experiment, the QDQWs are randomly oriented relative to the laser beams. For QDQWs with symmetry axes rotated by ψ relative to the laser beam, $\theta_F(E)$ is calculated similarly to Sec. II B from the matrix elements listed in Eq. (17). The experimentally more relevant expression for an ensemble of randomly oriented QDQWs is found by averaging over ψ . For E close to the absorption edge, the ensemble average $\bar{\theta}_F(E)$ is

$$\bar{\theta}_F(E) \simeq \frac{C' E I_1}{36} \sum_i [15|\alpha_{i,-3/2}|^2 + |\alpha_{i,-1/2}|^2 - 5|\alpha_{i,1/2}|^2 - 3|\alpha_{i,3/2}|^2 + 4\sqrt{3}(\alpha_{i,3/2}\alpha_{i,1/2} - \alpha_{i,-3/2}\alpha_{i,-1/2})] \frac{E - E_{X_i}}{(E - E_{X_i})^2 + \Gamma^2}, \quad (24)$$

where α_{i,F_z} are the expansion coefficients defined in Eq. (22). Transitions involving $2S_{3/2}$ and $3S_{3/2}$ are modified in an analogous way, but the expressions are omitted here for brevity. Note that the relative spectral weight of the individual terms changes compared to an oriented sample [Eq. (23)].

We next discuss how the TRFR signal amplitude, $\theta_F(E)$, changes with increasing asymmetry potential v_0 . Figure 4(a) shows the experimental data for $\theta_F(E)$ (symbols) and the absorption spectrum (dashed line) for the sample with $n_{\text{CdSe}} = 3$.¹³ Figures 4(b)–(d) show the calculated TRFR signal amplitudes (solid lines) for (b) $v_0 = 0$ meV, (c) $v_0 = 40$ meV, and (d) $v_0 = 70$ meV, respectively. The TRFR signal for random QDQW orientation is calculated from Eq. (24) taking into account transitions from the $1S_{3/2}$, $2S_{3/2}$, $3S_{3/2}$, and $1P_{3/2}$ valence band multiplets. The level broadening $\Gamma = 15$ meV was chosen to be comparable to the smallest linewidth in the experimental data. For the system with spherical symmetry, $v_0 = 0$ meV, the spectral weight of the resonance with the smallest energy is significantly larger than that of the two resonances at higher energies, in contrast to the experimental data. With increasing v_0 , the spectral weight is redistributed from the $1S_{3/2} - 1S_e$ transition to resonances involving other valence band multiplets, such that the spectral weight of the resonance with lowest energy approaches that of the higher-energy resonances [Figs. 4(c) and (d)]. The corresponding theoretical curves are in better qualitative agreement with the experimental results than the TRFR signal calculated for a spherically symmetric QDQW.

The single-particle level spectrum and transition matrix elements calculated above also allow one to calculate the absorption spectrum,

$$\text{abs}(E) \propto \sum_{|\Phi_c\rangle;|\Phi_v\rangle} |\langle \Phi_c | \hat{p}_x + i\hat{p}_y | \Phi_v \rangle|^2 \frac{\Gamma}{(E - E_X)^2 + \Gamma^2}. \quad (25)$$

The sum extends over all conduction and valence band states and E_X denotes the energy of the corresponding exciton transition. Close to the absorption edge, transitions from $|\Psi_{v,i}^{(SP)}\rangle$ and the $2S_{3/2}$ and $3S_{3/2}$ multiplets to $1S_e$ and $1P_e$, respectively, are dominant. The larger number of optically allowed transitions in the system with broken spherical symmetry [Fig. 3(b)] may also explain the absence of distinct peaks in the absorption spectrum, because transitions from p -type valence band states to $1P_e$ spectrally overlap with transitions from s -type valence band states to $1S_e$. In Figs. 4(b)–(d), we show the evolution of the absorption spectrum with increasing asymmetry of the QDQW (dashed lines) calculated using the same parameters as for the TRFR signal. While the TRFR signal is dominated by transitions involving $nS_{3/2}$ multiplets (Sec. II B), the absorption spectrum also involves transitions from excited valence band multiplets such as $1P_{1/2}$ and $2P_{3/2}$ which are neglected here. For the absorption spectrum, our calculations restricted to the $1S_{3/2}$, $2S_{3/2}$, $3S_{3/2}$, and $1P_{3/2}$ multiplets yield valid results only within ~ 0.15 eV of the absorption edge. For a QDQW with spherical symmetry, pronounced resonances are predicted to appear in the absorption spectrum close to the absorption edge [Fig. 4(b)]. For increasing v_0 , the redistribution of spectral weight effected by mixing of different valence band multiplets leads to a broadening of

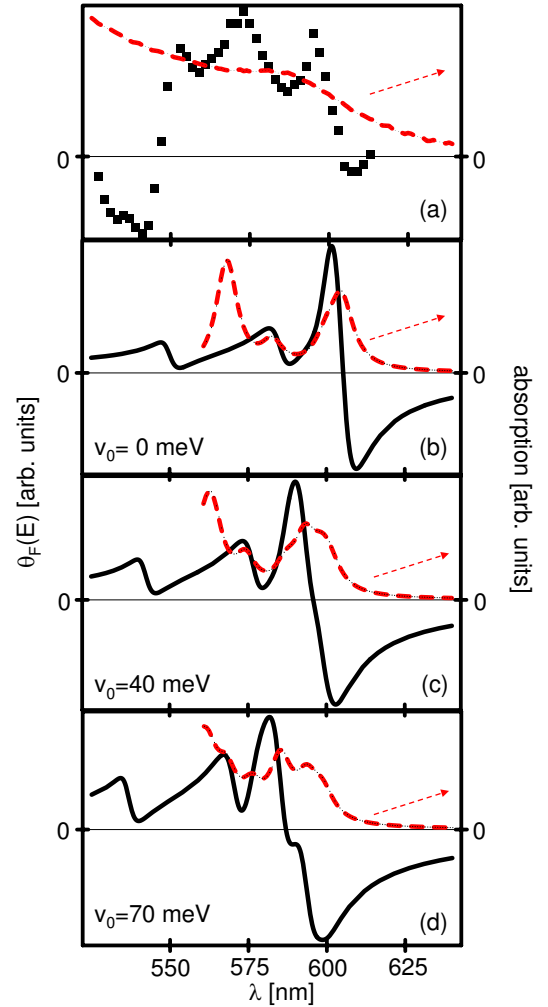


FIG. 4: (color online). (a) Experimental data for the amplitude of the TRFR signal, $\theta_F(E)$, measured at $T = 294$ K, and the optical absorption as a function of probe energy. (b)–(d) Calculated amplitude of the TRFR signal, $\theta_F(E)$, (solid line) and optical absorption (dashed line) for different strength of an anisotropy potential, $v_0 = 0, 40, 70$ meV, respectively. The calculation is restricted to the $1P_{3/2}$, $1S_{3/2}$, $2S_{3/2}$, and $3S_{3/2}$ valence band multiplets which dominate the optical response close to the absorption edge. For $\lambda < 560$ nm, transitions from higher valence band multiplets become important for the absorption spectrum and the restriction to only four valence band multiplets is no longer valid. Because $T = 294$ K is small compared to the conduction band level splitting, all electron spins are assumed to occupy $1S_e$ in the calculation of $\theta_F(E)$.

these resonances [Fig. 4(c)] which, ultimately, evolve into a step-like feature comparable to the experimental data [Fig. 4(d)].

However, for the small transition linewidth $\Gamma = 15$ meV chosen in Fig. 4(d), some resonance features can still be resolved in the theoretical absorption spectrum. One possible explanation for the discrepancy with exper-

imental data is that the linewidth of exciton transitions to $1P_e$ is larger than for $1S_e$ because of orbital relaxation from $1P_e$ to $1S_e$. We also point out that, for $v_0 \sim 70$ meV, the restriction of our analysis to only four valence band multiplets ($1S_{3/2}$, $2S_{3/2}$, $3S_{3/2}$, and $1P_{3/2}$) can no longer be justified rigorously. A calculation taking into account all multiplets in Fig. 1(f) would be required to yield rigorous results for the absorption spectrum in this regime of strong symmetry breaking.

From our analysis of a simple model for broken spherical symmetry, we conclude that mixing of different valence band multiplets redistributes the spectral weights in the Lehmann representation of $\theta_F(E)$ and accounts for a large number of resonances with comparable spectral weight (Fig. 4). Broken spherical symmetry is also consistent with a large Stokes shift and a featureless increase of the absorption spectrum.¹³

IV. SUMMARY AND DISCUSSION

Motivated by recent experiments,¹³ we have calculated the conduction and valence band states of CdS/CdSe/CdS QDQWs using $\mathbf{k} \cdot \mathbf{p}$ theory. The single-particle spectrum allowed us to evaluate the amplitude of the TRFR signal as a function of the probe energy, $\theta_F(E)$, for samples with well defined and random orientation of symmetry axes, respectively. For spherical QDQWs, $\theta_F(E)$ exhibits a pair of resonances for every $nS_{3/2}$ valence band multiplet [Fig. 2(b)], but does not correctly reproduce the spacing and spectral weight of the experimentally observed resonances. By contrast, a simple model with broken spherical symmetry reproduces the experimental data at least qualitatively.

For both the TRFR signal and the absorption spectrum, the model with broken spherical symmetry yields better agreement with experimental data than the calculations for a spherical QDQW (Fig. 4). However, the theoretical curve does not reproduce all experimental features and large values of v_0 are required in order to explain the experimental data. We, hence, re-emphasize that the discussion in Sec. III is only a qualitative analysis of TRFR for broken spherical symmetry. Additional theoretical work is required to improve the quantitative understanding of the energy level scheme of CdS/CdSe/CdS QDQWs and of the FR angle as a function of probe energy.

In particular, more realistic microscopic models for the variation of the QW width should be considered. Eight-band $\mathbf{k} \cdot \mathbf{p}$ calculations would allow one to quantify whether mixing of light and heavy hole states with the conduction and split-off band also reduces the spectral weight of the $1S_{3/2} - 1S_e$ exciton transition. If the full eight-band model gives results comparable to our description, this would further corroborate that spherical symmetry breaking must be taken into account to understand the level spectrum of CdS/CdSe/CdS QDQWs.¹⁶ Tight-binding calculations of the energy spectrum^{25,34,35} and $\theta_F(E)$ would allow one to explicitly include the atomistic structure of interfaces and to compare our calculations with a different theoretical framework.

Acknowledgments

This work was supported by ONR and DARPA. We acknowledge helpful discussion with J. Berezovsky, O. Gywat, W. Lau, and M. Ouyang.

-
- ¹ A. P. Alivisatos, J. Phys. Chem. **100**, 13226 (1996).
² A. P. Alivisatos, Science **271**, 933 (1996).
³ M. A. Hines and P. Guyot-Sionnest, J. Phys. Chem. **100**, 468 (1996).
⁴ B. O. Dabbousi, J. Rodriguez-Viejo, F. V. Mikulec, J. R. Heine, H. Mattoussi, R. Ober, K. F. Jensen, and M. G. Bawendi, J. Phys. Chem. B **101**, 9463 (1997).
⁵ A. R. Kortan, R. Hull, R. L. Opila, M. G. Bawendi, M. L. Steigerwald, P. J. Carroll, and L. E. Brus, J. Am. Chem. Soc. **112**, 1327 (1990).
⁶ A. Mews, A. Eychmüller, M. Giersig, D. Schooss, and H. Weller, J. Phys. Chem. **98**, 934 (1994).
⁷ A. Mews, A. V. Kadavanich, U. Banin, and A. P. Alivisatos, Phys. Rev. B **53**, R13242 (1996).
⁸ Y. C. Tian, T. Newton, N. A. Kotov, D. M. Guldi, and J. H. Fendler, J. Phys. Chem. **100**, 8927 (1996).
⁹ R. B. Little, M. A. El-Sayed, G. W. Bryant, and S. Burke, J. Chem. Phys. **114**, 1813 (2001).
¹⁰ D. Battaglia, J. J. Li, Y. Wang, and X. Peng, Angew. Chem. Int. Ed. **42**, 5035 (2003).
¹¹ J. A. Gupta, D. D. Awschalom, X. Peng, and A. P. Alivisatos, Phys. Rev. B **59**, R10421 (1999).
¹² J. A. Gupta, D. D. Awschalom, Al. L. Efros, and A. V. Rodina, Phys. Rev. B **66**, 125307 (2002).
¹³ J. Berezovsky, M. Ouyang, F. Meier, D. D. Awschalom, D. Battaglia, and X. Peng, cond-mat/0411181.
¹⁴ J. Li and L.-W. Wang, Appl. Phys. Lett. **84**, 3648 (2004).
¹⁵ W. Jaskólski and G. W. Bryant, Phys. Rev. B **57**, R4237 (1998).
¹⁶ E. P. Pokatilov, V. A. Fonoberov, V. M. Fomin, and J. T. Devreese, Phys. Rev. B **64**, 245328 (2001).
¹⁷ *Numerical Data and Functional Relationships in Science and Technology*, Landolt-Börnstein, New Series, Group III, Vol. 41, Subvolume B (Springer, Heidelberg, 1999).
¹⁸ S.-H. Wei, S. B. Zhang, and A. Zunger, J. Appl. Phys. **87**, 1304 (2000).
¹⁹ X. Peng, M. C. Schlamp, A. V. Kadavanich, and A. P. Alivisatos, J. Am. Chem. Soc. **119**, 7019 (1997).
²⁰ T. Richard, P. Lefebvre, H. Mathieu, and J. Allègre, Phys. Rev. B **53**, 7287 (1996).
²¹ While the numerical values for the CdS Luttinger parameters given in the literature vary widely, the results for $\theta_F(E)$ remain qualitatively the same for different values of $\gamma_{1,CdS}$ and γ_{CdS} .

- ²² J.-B. Xia, Phys. Rev. B **40**, 8500 (1989).
- ²³ Al. L. Efros, Phys. Rev. B **46**, 7448 (1992).
- ²⁴ D. Schooss, A. Mews, A. Eychemüller, and H. Weller, Phys. Rev. B **49**, 17072 (1994).
- ²⁵ G. W. Bryant and W. Jaskólski, Phys. Rev. B **67**, 205320 (2003).
- ²⁶ D. J. Norris, Al. L. Efros, M. Rosen, and M. G. Bawendi, Phys. Rev. B **53**, 16347 (1996).
- ²⁷ Al. L. Efros and M. Rosen, Phys. Rev. B **58**, 7120 (1998).
- ²⁸ S. Hugonnard-Bruyère, C. Buss, F. Vouilloz, R. Frey, and C. Flytzanis, Phys. Rev. B **50**, 2200 (1994).
- ²⁹ N. Linder and L. J. Sham, Physica E **2**, 412 (1998).
- ³⁰ L. J. Sham, J. Mag. Mag. Mat. **200**, 219 (1999).
- ³¹ F. Meier, V. Cerletti, O. Gywat, D. Loss, and D. D. Awschalom, Phys. Rev. B **69**, 195315 (2004).
- ³² J. M. Luttinger and W. Kohn, Phys. Rev. **97**, 869 (1955).
- ³³ We have extended the diagonalization of the $\delta V(\mathbf{r})$ to include the $1D_{5/2}$ multiplet, but the agreement with experimental data did not improve further. The qualitative behavior of both $\theta_F(E)$ and the absorption spectrum remains comparable to the results obtained from the analysis of the $1S_{3/2}$ and $1P_{3/2}$ multiplets.
- ³⁴ J. Pérez-Conde and A. K. Bhattacharjee, Phys. Status Solidi B **229**, 485 (2002).
- ³⁵ R.-H. Xie, G. W. Bryant, S. Lee, and W. Jaskólski, Phys. Rev. B **65**, 235306 (2002).